CrystEngComm

ROYAL SOCIETY OF CHEMISTRY

PAPER

View Article Online
View Journal

Cite this: DOI: 10.1039/c9ce01584a

Crystallization of Ge in ion-irradiated amorphous-Ge/Au thin films

G. Maity,[a] S. Ojha,[b] S. Dubey,[c] P. K. Kulriya,[b] I. Sulania,[b] S. Dhar,[d] T. Som,[e] D. Kanjilal[b] and Shiv P. Patel *[a]

Received 8th October 2019,
Accepted 22nd November 2019

DOI: 10.1039/c9ce01584a

rsc.li/crystengcomm

Herein, the structural, optical, and electrical properties of Au-induced crystallization in amorphous germanium (a-Ge) thin films are presented for future solar energy material applications. The a-Ge/Au thin films on quartz substrate were prepared *via* the e-beam and thermal evaporation techniques, respectively. The as-prepared samples were irradiated with 100 MeV Ni^{7+} ions at different fluences of 1×10^{12} ions per cm^2, 5×10^{12} ions per cm^2, 1×10^{13} ions per cm^2 and 5×10^{13} ions per cm^2. The ion irradiation did not result in the crystallization of Ge; instead, an increase in ion fluence decreased the Au crystallite size, which ultimately deteriorated the Au crystallization. The ion-irradiated samples were post-annealed for 4 h at a fixed temperature of 300 °C to achieve the crystallization of Ge. The post-annealing of the ion-irradiated samples led to the crystallization of Ge, where the crystallization of Ge was better for the samples irradiated at high fluence, leading to a smaller grain size corresponding to a high grain boundary, and hence high defect sink density. The energy bandgap of crystalline Ge was determined using reflectance and transmittance spectra, which was found to be low (~0.64 eV) at higher fluence. The field-emission scanning electron microscopy and atomic force microscopy analyses show that the surface microstructure changed for the post-annealed samples irradiated at different fluences. The role of the fractal-like surface microstructure in multiple scattering of light on the film surface is discussed. Thus, the lower values of resistivity and sheet resistance as well as good optical properties of Ge make it a promising material for future poly-Ge-based solar cell applications.

I. Introduction

The polycrystalline Ge is an important material for the fabrication of low-cost semiconductor devices, such as thermo-photovoltaics,[1] and bottom cells of tandem and multi-junction cells[2] to convert solar radiation into electrical energy. In the field of crystallization, significant attention has been paid to solid-phase crystallization (SPC).[3] SPC is usually accomplished by annealing a material at a very high temperature for a considerably long time. For instance, Ge crystallization is achieved after annealing amorphous Ge at 375 °C for a long period.[4,5] On the other hand, amorphous germanium (a-Ge) films in contact with some metals (Al, Au, Cu, Ag, Ni, *etc.*) may be crystallized at a low temperature (160–300 °C), resulting in polycrystalline-Ge films.[6–12] This process is known as metal-induced crystallization (MIC). The crystallization temperature (T_{cryst}) of a-Ge reduces significantly to 250 °C when it is kept in contact with Au,[13] and this process is known as gold-induced crystallization (GIC).[13,14] GIC results in substantially faster crystal growth than SPC, and at a lower annealing temperature. Consequently, researchers have put more efforts into reducing the crystallization temperature of a-Ge under thermal annealing conditions by changing different parameters (such as deposition temperature, and interface oxide layer), with the objective to advance the quality of c-Ge-based solar cells. Wang *et al.*[15] studied the effect of Al grain size on the crystallization of a-Si films. In their investigation, Al thin films of various thicknesses were deposited on different substrates and the annealing process was used to vary the grain size of Al.[15] The crystallinity of a-Si was significantly improved due to the presence of the smaller Al grain size, where the grain boundary density was higher. Recently, Nakata *et al.*[16] studied the Al-induced crystallization of Ge thin films by varying the Al grain size. The metal-induced crystallization growth velocity of the Ge film was found to decrease with an increase in Al grain size. A careful review of the literature suggests that the effects of Au

[a] *Department of Pure and Applied Physics, Guru Ghasidas Vishwavidyalaya (A Central University), Bilaspur 495009, India. E-mail: shivpoojanbhola@gmail.com*
[b] *Inter University Accelerator Centre, Aruna Asaf Ali Marg, New Delhi 110067, India*
[c] *Department of Physics, School of Engineering, University of Petroleum and Energy Studies, Bidholi, Dehradun-248007, India*
[d] *Department of Physics, Shiv Nadar University, Gautam Buddha, Nagar-201314, India*
[e] *Institute of Physics, Sachivalaya Marg, Bhubaneswar-751005, India*

crystallite (*i.e.* grain) size on the nucleation and growth of polycrystalline Ge has not been reported to date to the best of our knowledge. In this respect, swift heavy ion (SHI) irradiation is known to be the best tool to tailor the size of the crystallites in Au thin films.[17,18] Therefore, it is of great importance to attempt investigating the effects of Au crystallite size on the nucleation and growth of polycrystalline Ge at low temperatures in a controlled fashion.

In the present work, the effect of ion irradiation on the Au-induced crystallization of a-Ge at a low temperature (300 °C) is presented. Specifically, 50 nm a-Ge and 50 nm crystalline Au bilayer films (*i.e.* a-Ge/Au) were prepared on ultrasonically cleaned quartz substrates using the e-beam evaporation and thermal evaporation techniques, respectively. The as-prepared a-Ge/Au/quartz samples (*i.e.* pristine) were irradiated with 100 MeV Ni^{7+} ions at different fluences of 1×10^{12} ions per cm^2, 5×10^{12} ions per cm^2, 1×10^{13} ions per cm^2, and 5×10^{13} ions per cm^2 at room temperature (RT). The ion irradiation led to a systematic decrease in Au crystallites with an increase in ion fluence, but it did not lead to the crystallization of Ge. To achieve the crystallization of a-Ge, the ion-irradiated samples were post-annealed at a temperature of 300 °C. The crystallization of a-Ge was found to be better for the samples that were irradiated at higher fluence. The optical and electrical properties were also studied to extend the research scope for the possible improvement of the solar cell design.

In section II, we present the experimental details followed by section III, in which the results are discussed. Finally, the conclusions are presented in section IV.

II. Experimental details

The a-Ge (50 nm)/Au (50 nm) bilayer films were deposited on ultrasonically cleaned quartz substrates using the e-beam evaporation and thermal evaporation techniques, respectively, in a high vacuum ($\sim 6 \times 10^{-7}$ mbar) chamber without breaking the vacuum. The bilayer films were irradiated by 100 MeV Ni ions with the different fluences of 1×10^{12} ions per cm^2, 5×10^{12} ions per cm^2, 1×10^{13} ions per cm^2, and 5×10^{13} ions per cm^2 at RT using the 15 UD tandem Pelletron accelerator facility at the Inter-University Accelerator Centre (IUAC), New Delhi, India. To prevent sample heating during ion irradiation, the ion flux was kept at about $\sim 10^{11}$ ions per cm^2 s. The ion beam was continuously scanned over the entire film using a beam scanner. The electronic energy loss (S_e) and nuclear energy loss (S_n) values for 100 MeV Ni ions in the Au film were 23.69 keV nm^{-1} and 0.061 keV nm^{-1}, respectively, and that for the Ge film was 11.13 keV nm^{-1} and 0.023 keV nm^{-1}, respectively, as calculated from the stopping and range of ions in matter (SRIM) code.[19] To achieve the crystallization of a-Ge, the ion-irradiated samples were post-annealed at 300 °C in a tubular furnace for 4 h in the presence of an N_2 atmosphere. The crystalline structure of the samples was determined *via* X-ray diffraction (XRD) measurement using a D8 Advance Bruker with a Cu K-alpha source. Raman spectra were recorded using a Renishaw microscope with 514 nm He–Ne laser excitation. To get further information about atomic diffusion at the interface, a Rutherford backscattering spectrometry (RBS) experiment was carried out using 1.7 MeV He^+ ions at IUAC, New Delhi. The RBS data was analyzed by using the XRUMP simulation code.[20] To study the optical properties of the post-annealed samples, UV-visible spectroscopy was performed using a UV-vis-NIR spectrophotometer (Shimadzu-3101PC, Japan) with unpolarized light. The surface microstructure of the samples was studied by field-emission scanning electron microscopy (FE-SEM) measurement using a JSM-7610F Schottky field-emission scanning electron microscope with the energy of 15 keV. Energy dispersive X-ray spectroscopy (EDX) was performed using 5 keV energy to detect the elements present on the surface and subsurface region. The electrical resistivity of the samples was measured by Hall-measurement using a Hall-effect measurement system (HMS-3000) with a magnetic field of 0.57 Tesla. The surface topography of the films was studied by atomic force microscopy with a Nanoscope IIIa in tapping mode, using silicon probes having a diameter of ~10 nm.

III. Results and discussions

A. Structural properties

Fig. 1(a) shows the XRD pattern of the pristine and ion-irradiated samples. There are two diffraction peaks at about $2\theta \sim 38.21°$ and 44.54° in the pristine sample, corresponding to the (111) and (200) diffraction lattice planes of Au, respectively. The Au (111) peak intensity was found to decrease with an increase in the ion fluence, which may be due to the decrease in the crystallinity of the Au film.[17,18] It was also observed that the full width at half maximum (FWHM) of the Au diffraction peaks increased with an increase in ion fluence (shown in Fig. 1(b)). This observation may be attributed to the decrease in the crystallites size (*i.e.* grain size) of the Au film.[18] The crystallite size of Au was estimated by using the Debye–Scherrer formula,[21] which was found to be 14.0 nm, 13.0 nm, 12.0 nm, 11.0 nm, and 10.0 nm, corresponding to the pristine and ion irradiated samples at different fluences of 1×10^{12} ions per cm^2, 5×10^{12} ions per cm^2, 1×10^{13} ions per cm^2, and 5×10^{13} ions per cm^2, respectively. Therefore, the XRD results of ion irradiated a-Ge/Au thin films clearly depict that the crystallite size in the Au films decreased with an increase in ion fluence, which led to a systematic increase in the grain boundary density in the Au films under ion irradiation. It is well known that the grain boundaries and the bilayer interface act as defect sinks.[22] Therefore, it can be concluded that the defect sink density is higher in the samples irradiated at higher fluences than the samples irradiated at a lower fluence. It should be noted here that by changing the defect sink density at a desired location with the help of ion irradiation, the kinetics of Ge crystal growth could be altered.

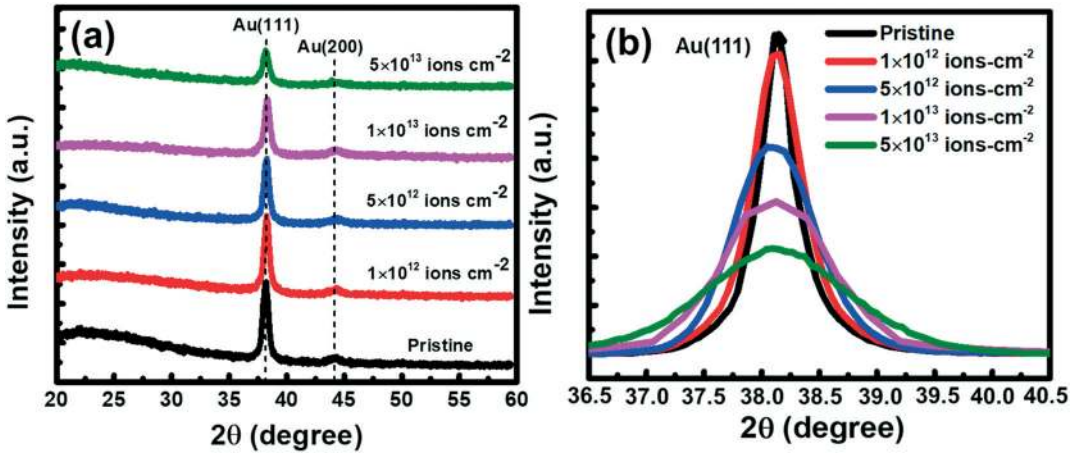

Fig. 1 (a) XRD pattern of a-Ge/Au pristine and ion-irradiated thin films at different fluences of 1×10^{12} ions per cm^2, 5×10^{12} ions per cm^2, 1×10^{13} ions per cm^2, and 5×10^{13} ions per cm^2 and (b) variation of FWHM of Au (111) diffraction peak with ion fluence.

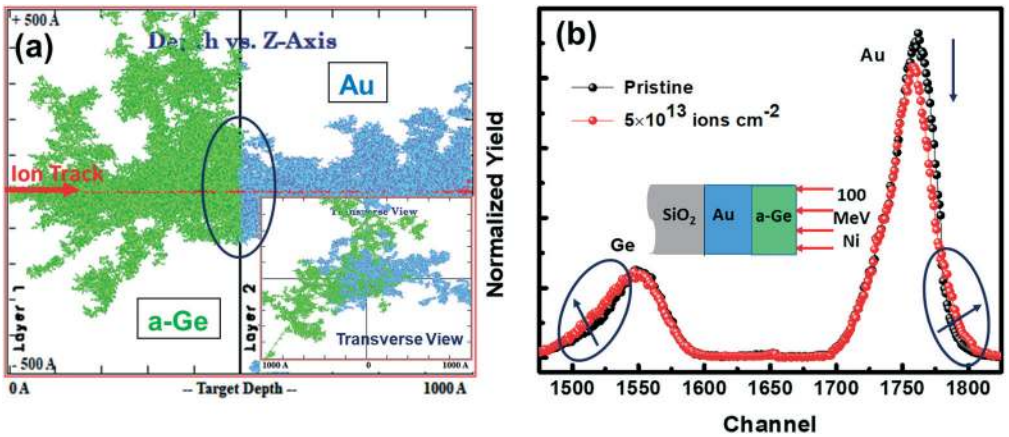

Fig. 2 (a) TRIM simulation of (depth *vs.* *Z*-axis) a-Ge (*i.e.* layer 1 colored by green) and Au (*i.e.* layer 2 colored by blue) at the interface (mixing region shown by ring). The inset shows the transverse view of the TRIM simulation. (b) RBS spectra of the pristine and ion-irradiated a-Ge/Au thin film at a fluence of 5×10^{13} ions per cm^2.

Fig. 2(a) shows the transport and range of ions in matter (TRIM) simulation[19] of the ion trajectories (depth *vs.* *Z*-axis) at the a-Ge (layer 1 colored by green) and Au (layer 2 colored by blue) interface. The marked region (*i.e.* inside ring) at the interface clearly shows the interlayer atomic diffusion of the Ge and Au atoms. The inset of Fig. 2(a) shows the transverse view ion trajectories, which clearly evidence the interlayer diffusion of Ge and Au. The RBS measurements were carried out to observe the inter-diffusion of Ge and Au atoms at the a-Ge/Au interface. Fig. 2(b) shows the RBS spectra of the pristine sample and sample irradiated at a fluence of 5×10^{13} ions per cm^2. The pristine sample shows a sharp interface for the Au and Ge layer in the RBS spectra. However, the RBS spectrum measured for the ion-irradiated sample clearly shows the inter-diffusion of Ge and Au atoms across their interface region.[23]

As shown previously in Fig. 1, the XRD pattern of the pristine and ion-irradiated samples do not show any diffraction peak corresponding to crystalline Ge. To achieve Ge crystallization, all the ion-irradiated samples were post annealed at 300 °C in a tubular furnace for 4 h in the presence of an N_2 atmosphere. Fig. 3(a) shows the XRD patterns of the post-annealed samples irradiated at different fluences. It can be seen that two diffraction peaks at around 2θ ~27.56° and 53.87° corresponding to the Ge (111) and Ge (311) lattice planes appeared in the sample irradiated at a fluence of 1×10^{12} ions per cm^2.[24] As the ion fluence increased to 1×10^{13} ions per cm^2, one more diffraction peak at around 45.45° corresponding to the Ge (220) diffraction plane also appeared. Upon further increasing the fluence to 5×10^{13} ions per cm^2, another new diffraction peak appeared at around 36.66°, corresponding to the (221) lattice plane of Ge. Therefore, the XRD measurement confirms the crystallization of a-Ge due to thermal annealing after ion irradiation as well as the polycrystalline nature of the crystallized Ge. It is also observed that the XRD peak

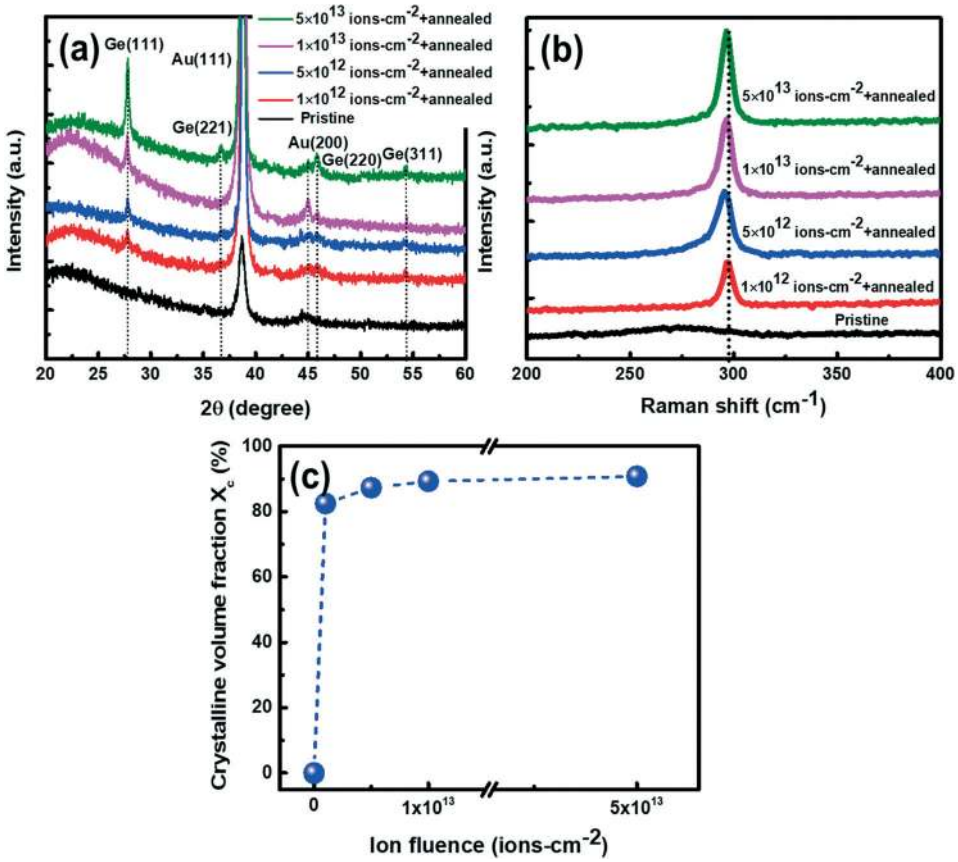

Fig. 3 (a) XRD pattern and (b) Raman spectra of the pristine sample and samples post-annealed (after ion irradiation at different fluences) at 300 °C. The XRD and Raman results clearly show the crystallization of Ge due to thermal annealing treatment after ion irradiation. (c) Crystalline volume fraction of Ge after post-annealing of ion-irradiated samples.

intensity corresponding to the Ge (111) lattice plane increases with ion irradiation fluence. The increase in the Ge diffraction peak intensity indicates the better crystallinity of Ge in the post-annealed samples, which were irradiated at a higher fluence. This can be understood based on the Au crystallite size or density of the grain boundaries. It was observed that ion irradiation of the a-Ge/Au samples at higher fluences led to a decrease in the Au crystallite size, which caused the grain boundary density (*i.e.* increase in defect sink density) to increase. It was also observed that ion irradiation led to the diffusion of Ge and Au atoms near the interface region. Therefore, thermal treatment (*i.e.* post-annealing) of the ion-irradiated samples provides enough energy and more space to the free Ge atoms to diffuse *via* the vacancy mechanism along the Au grain boundaries and bilayer interface, which act as defect sinks.[15,16,22] An increasing number of Ge atoms reach near the grain boundaries to initiate the formation of the nucleus of a new c-Ge phase, which is thermodynamically favorable since it reduces the overall free energy of the system. In the case of the samples irradiated at a higher fluence, the resulting higher grain boundary density led to higher crystallinity of Ge. Fig. 3(b) shows the Raman spectra of the pristine and post-annealed samples irradiated at different fluences. A Raman peak at about 300 cm^{-1} is observed for the all post-annealed samples irradiated at different fluences. This corresponds to the vibrational mode of the Ge–Ge bond of c-Ge.[13,14] The Raman peak intensity was found to increase with an increase in ion fluence, which reveals the better crystallization of Ge in the samples irradiated at higher ion fluences (in concordance with the XRD results). The slight shift in the Raman peak position towards lower frequencies with an increase in fluence can be attributed to the increase in the density of grains.[25] For a quantitative analysis of crystallinity, the crystalline volume fraction (X_c) was calculated using the formula: $X_c = \frac{I_c}{I_c + \alpha I_a}$, where I_c and I_a denote the crystalline and amorphous integral intensities near 300 cm^{-1} and 270 cm^{-1}, respectively.[26] The photo absorption correction factor (α) was assumed to be 0.8.[27] The X_c values were found to increase from 82.48% to 90.78% for the post-annealed sample irradiated at different fluences, as shown in Fig. 3(c). Therefore, based on the above observations, it can be concluded that the size of the Au crystallites controls the nucleation and growth of the polycrystalline Ge in the present investigation. To explore the tunable properties and possible applications of the polycrystalline Ge as a solar energy material, FESEM, AFM,

UV-visible transmittance and electrical measurements were performed and discussed in the following subsections.

B. Surface properties

To gain some understanding of the surface microstructure of the thin films, FESEM measurements were carried out on the pristine and post-annealed samples irradiated at different fluences. Fig. 4(a–e) show the surface microstructure of the pristine and post-annealed samples irradiated at different fluences. The pristine sample is composed of a uniform dot microstructure, and post-annealing of the ion-irradiated samples led to particle growth. Fig. 4(f) shows the EDX spectra of the pristine and post-annealed samples irradiated at different fluences. Only Ge was observed on the surface of the pristine sample. The post-annealing of the ion-irradiated samples resulted in an increase in the Au peak (at 1.19 keV) intensity at the cost of the Ge peak (at 2.15 keV) intensity, which clearly indicates the exchange of the Au and Ge atoms due to post-annealing.[28] The increasing in Au concentration on the surface with an increase in ion fluence (post-annealed at fixed temperature of 300 °C) is shown in the inset figure. The Au concentration was found to around 20% in the Ge layer. AFM measurements were also carried out on the pristine and post-annealed samples irradiated at different fluences for a greater understanding of the surface microstructure and topography.

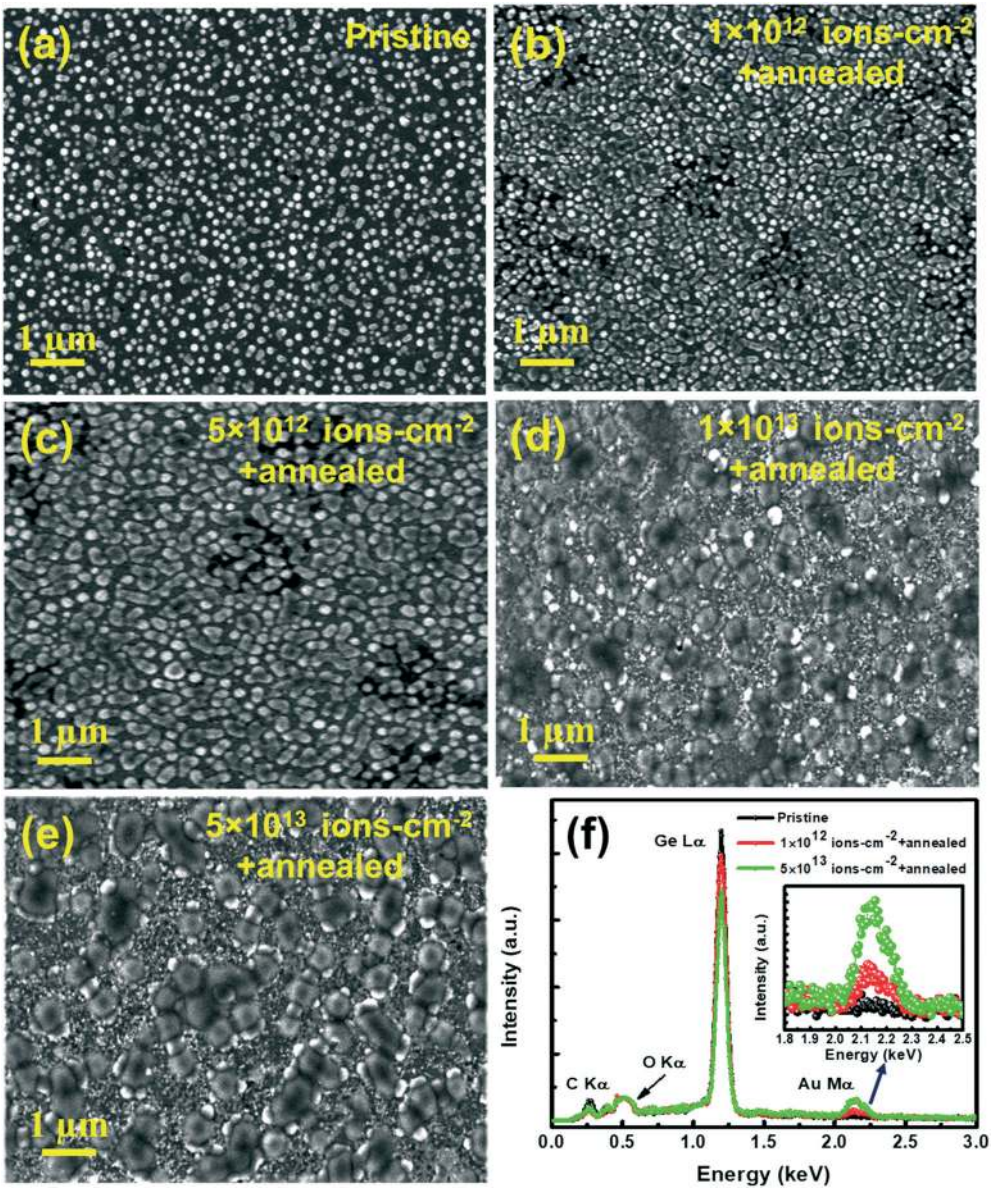

Fig. 4 FE-SEM images of (a) pristine sample and samples post-annealed at 300 °C after ion irradiation at different fluences of (b) 1×10^{12} ions per cm^2, (c) 5×10^{12} ions per cm^2, (d) 1×10^{13} ions per cm^2, and (e) 5×10^{13} ions per cm^2. (f) EDX spectra of pristine sample and post-annealed (at 300 °C) samples irradiated at a fluence of 1×10^{12} and 5×10^{13} ions per cm^2.

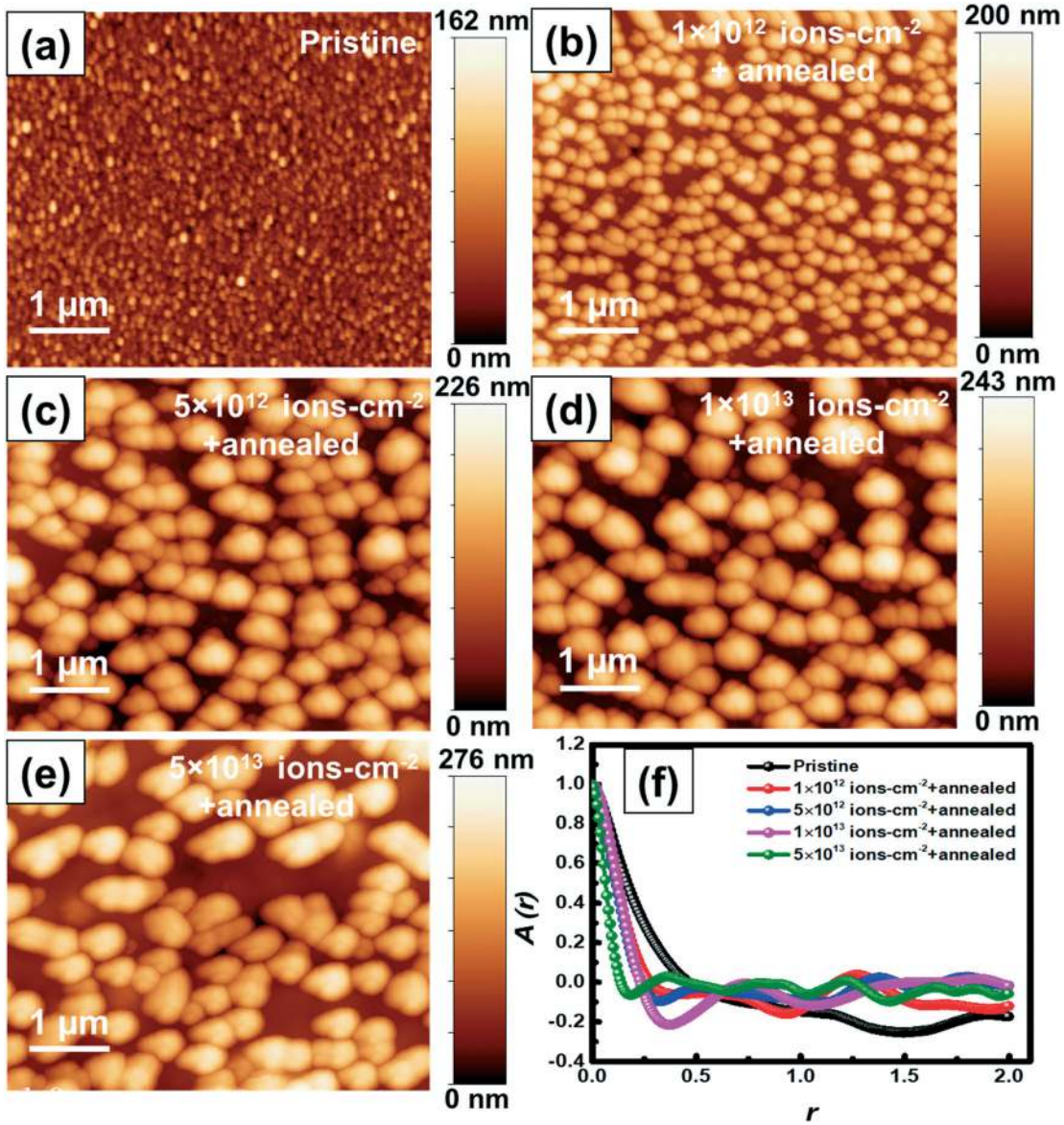

Fig. 5 Two-dimensional AFM images of (a) pristine sample, and samples post-annealed at 300 °C after ion irradiation at different fluences of (b) 1 × 10^{12} ions per cm^2, (c) 5 × 10^{12} ions per cm^2, (d) 1 × 10^{13} ions per cm^2, and (e) 5 × 10^{13} ions per cm^2. (f) One-dimensional autocorrelation function $A(r)$ as a function of r of the pristine sample and samples post-annealed at 300 °C after ion irradiation at different fluences.

Fig. 5(a–e) show the 2D AFM images of the pristine and post-annealed irradiated samples. The pristine sample showed smaller particles with an average size of 112 nm and the particle size was observed to increase further with an increase in ion fluence after post-annealing. The average particle size was found to be 168 nm, 285 nm, 425 nm, and 489 nm after post-annealing of the samples irradiated at different fluences of 1 × 10^{12} ions per cm^2, 5 × 10^{12} ions per cm^2, 1 × 10^{13} ions per cm^2, and 5 × 10^{13} ions per cm^2, respectively (summarized in Table 1). This is in accordance

Table 1 The fractal parameters such as average particle size, average roughness (R_a), RMS roughness (R_q), roughness exponent (α), and fractal dimension (D_f)

Sample details	Average particle size (nm)	Average roughness (nm)	RMS roughness (nm)	Roughness exponent (α)	Fractal dimension (D_f)
Pristine	112	2.54 ± 0.26	6.88 ± 0.10	0.93	2.07
1 × 10^{12} ion-cm^{-2} + annealed at 300 °C	168	31.61 ± 0.46	36.65 ± 0.41	0.88	2.12
5 × 10^{12} ion-cm^{-2} + annealed at 300 °C	285	34.24 ± 0.38	40.72 ± 0.37	0.85	2.15
1 × 10^{13} ion-cm^{-2} + annealed at 300 °C	425	39.29 ± 0.32	46.19 ± 0.25	0.83	2.17
5 × 10^{13} ion-cm^{-2} + annealed at 300 °C	489	42.10 ± 0.17	54.93 ± 0.19	0.82	2.18

with the average sizes observed from the FESEM images. The root mean square (rms) roughness (R_q) was found to increase with an increase in the ion fluence in the post-annealed samples. It should be noted here that the high surface roughness may be helpful in optical absorption applications, which is very important for solar cells. Fractal analysis of the AFM images was carried out mainly to get a deeper understanding of the surface morphology. These analyses significantly simplify the descriptive properties of the surface. One analysis is to understand the distribution of the heights of different points on the surface, and the correlations between them.[29] The correlation between the heights of the various surface points was accomplished with the help of an autocorrelation function. Fig. 5(f) shows the one-dimensional autocorrelation function $A(r)$ as a function of r of the pristine and post-annealed samples irradiated at different fluences. The exponentially decreasing behavior of the autocorrelation function confirms that the investigated surface has a self-affine nature and fractal were formed on the surfaces.[30] The calculated fractal parameters are summarized in Table 1. The fractal dimension (D_f) of the surface was found to increase from 2.07 to 2.18. Thus, to understand the importance of the fractal surfaces in the scattering of light, the Berry and Percival assumptions were studied in detail.[31] The basic simplifying assumption considered by Berry and Percival is that multiple scattering effects provide a limiting condition on a suitable combination of fractal dimension (D_f) and number of constituent particles (N) on the surface that participate in the scattering process.[31] Intuitive considerations suggest that, when $D_f < 2$, single-scattering effects are predominant at all the values of N. On the contrary, for $D_f > 2$, approximate estimates show that multiple scattering is not always negligible.[31] In the present study, since the fractal dimensions are slightly greater than 2, we may need to consider multiple scattering. According to Berry and Percival,[31] the scattering cross section for the whole system is proportional to a power of the total number of particles. For $D_f > 2$, the scattering cross section (σ_{sca}) follows the equation $\sigma_{sca} \propto N^{\left(2-\frac{2}{D_f}\right)}$, where N is the number of particles. A Matlab program was used to calculate the scattering cross sections in the present work. Fig. 6(a) shows the calculated σ_{sca} for the fractal dimension ranging from 2.07 to 2.18. In particular, for all cases, we considered that N (which depends on the size of the system) ranges from 0 to 1000. The results represent that when N tends to zero, σ_{sca} goes to zero as well, *i.e.* multiple scattering of light is not present. The calculated σ_{sca} values were found to increase with an increase in N. Thus, the value of N is very important for multiple scattering of light. The trend of the graph (shown by arrow) indicates that σ_{sca} increases with an increase in D_f. Therefore, a good polycrystalline-Ge sample with high values of σ_{sca} (*i.e.* high D_f value) was fabricated using ion irradiation and post-annealing processes. The three dimensional AFM image of the post-annealed sample irradiated at a fluence of 5×10^{13} ions per cm^2 is shown in Fig. 6(b), which demonstrates a schematic of multiple scattering of light on a fractal surface. The multiple scattering behavior of light on fractal surfaces will benefit more light absorption, which may be applicable in advanced solar cell devices.[32]

C. Optical properties

The optical properties of the pristine and post-annealed samples (after ion irradiation) were studied using UV-visible spectroscopy measurements. Fig. 7(a) and (b) show the reflectance (R) and transmittance (T) spectra, respectively, of the pristine and post-annealed samples irradiated at different fluences. The reflectance spectrum (Fig. 7(a)) is divided in two regions, region-1 (wavelength less than 700 nm) and region-2 (wavelength greater than 700 nm). In region-2, the reflectance spectra show oscillatory behavior due to the interference of light, depicting the incomplete absorption. Region-1 is more important to generate free electrons in solar

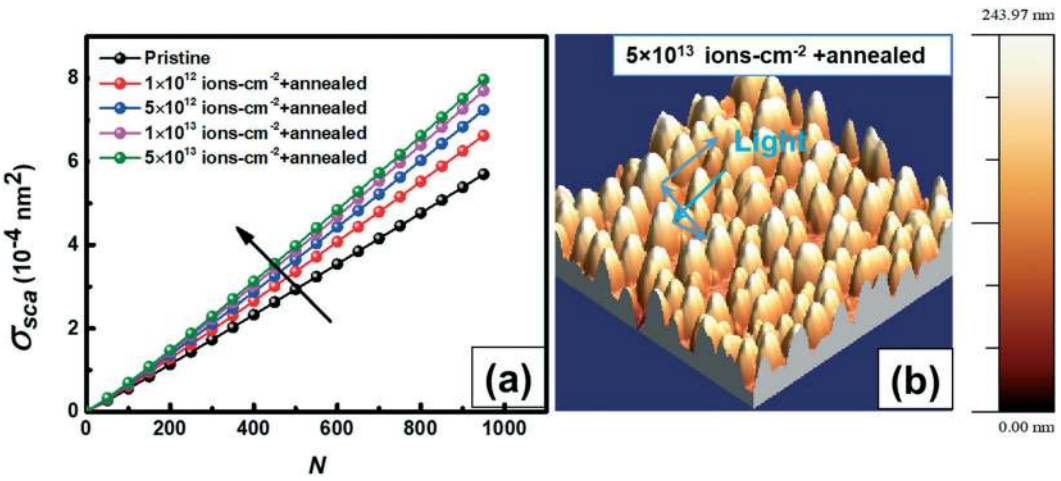

Fig. 6 (a) Scattering cross section (σ_{sca}) as a function of number of constituent grains (N) on film surface and (b) three-dimensional AFM image of the post-annealed (at 300 °C) sample irradiated at a fluence of 5×10^{13} ions per cm^2, schematically demonstrating the multiple scattering of light.

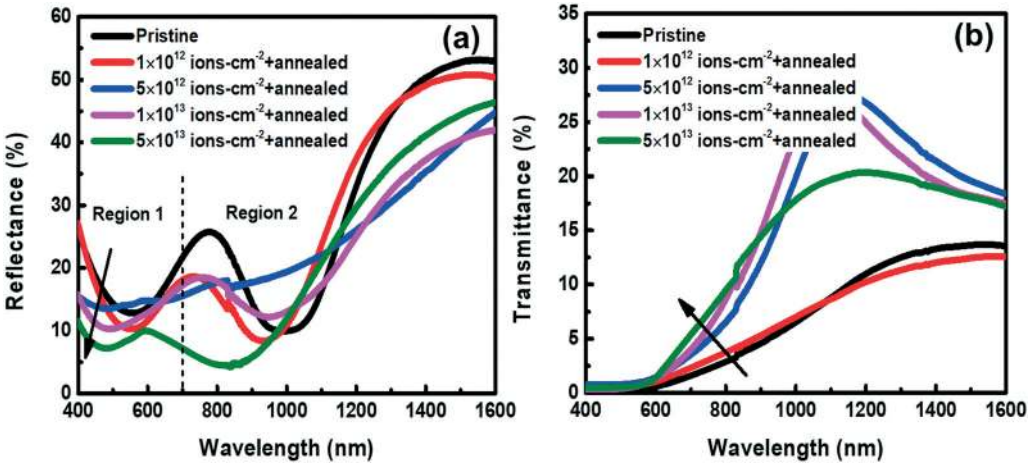

Fig. 7 (a) Reflectance and (b) transmittance spectra of pristine sample and post-annealed (at 300 °C) samples after ion irradiation at different fluences.

cells, which shows the decreasing behavior of reflectance. The reflectance spectra of region-1 strongly depend on the crystallinity of the surface and sub-surface regions of the film.[33] In case of the pristine sample, the reflectance is higher because the disorder present in a-Ge and Au acts as a mirror layer. The post-annealing of the ion-irradiated samples led to the crystallization of Ge, and crystallization increased with an increase in ion fluence. As a result, the reflectance decreased with an increase in ion fluence in the case of the post-annealed samples, as indicated by an arrow in the figure. Fig. 7(b) shows the transmittance spectra of the pristine and post-annealed samples. The pristine sample shows no oscillation and it has very low transmittance of light since the Au film acts as a barrier for transmitting the light. The post-annealed samples irradiated at different fluences show oscillatory behavior due to the interference of light. This may be due to the atomic exchange process (diffusion of Au and Ge atoms at the interface) during the crystallization of Ge.[34,35] A blue shift in the transmittance spectra was observed. The blue shift in transmittance and the decreasing behavior in the reflectance spectra suggest the improvement in Ge crystallinity, where Au does not act as a mirror layer due to the mixing of Au and Ge.[33,35] The nature of both spectra (*i.e.* reflectance and transmittance) may also be due to the increase of multiple scattering of light on the surface of the film. The absorption coefficient (α) was calculated using the equation $\alpha = \frac{1}{t}\ln\left(\frac{1-R}{T}\right)$ where, t is the thickness of the bilayer film. Fig. 8(a) shows the absorption coefficient curve for the pristine and post-annealed samples irradiated at different fluences. It is observed that the absorption coefficient decreases in the visible and near infrared regions, which is indicated by an arrow in the spectra. There is a tailing in the absorption coefficient spectra, which is due to the presence defect states in the energy band gap of the pristine Ge film. The tailing in the absorption gets sharper for the post-annealed samples irradiated at different fluences, indicating the phase

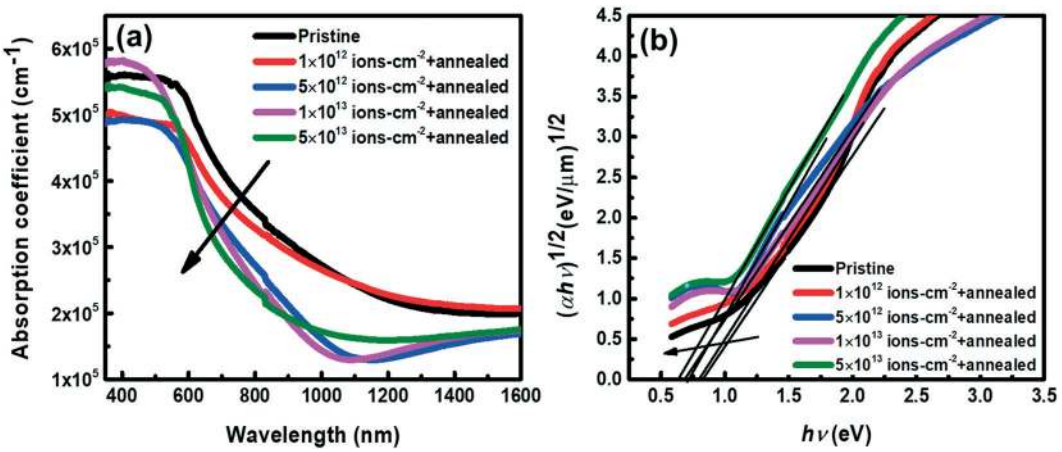

Fig. 8 (a) Absorption coefficient and (b) plot of $(\alpha h\nu)^{1/2}$ *vs.* photon energy ($h\nu$) for the pristine sample and post annealed (at 300 °C) samples after ion irradiation at different fluences.

transition from a-Ge to crystalline (c)-Ge. The optical band gap of the bilayer systems was estimated using Tauc's equation: $(\alpha h\nu)^{1/n} = B(h\nu - E_g)$, where $h\nu$ is the photon energy, α is the absorption coefficient, B is the edge width, E_g is the energy band gap, and n is the exponent (which is 2 for Ge).[36] Fig. 8(b) shows the Tauc plot of $(\alpha h\nu)^{1/2}$ *vs.* $h\nu$ of the bilayer system for the pristine and post-annealed samples irradiated at different fluences. The linear portion of the Tauc plot was extrapolated to yield the optical band gap at a zero value of $(\alpha h\nu)^{1/2}$. The band gap was found to decrease with an increase in ion fluence for the post-annealed samples, as indicated by the arrow in the figure. The post-annealing of the ion-irradiated samples resulted in the crystallization of Ge and a simultaneous decrease in the band gap from 0.85 eV to 0.64 eV (summarized in Table 2). This may be due to the fact that Au introduces energy states in the original band gap of Ge because of the diffusion of Au in Ge, or it may be due to some other factors.[35,37] The decrease in the energy band gap after the crystallization of Ge indicates that more defect states were introduced by Au in Ge and reduction of the defect states of Ge during the crystallization process.

D. Electrical properties

Fig. 9(a) and (b) show the variation in the electrical resistivity (ρ) and sheet resistance (R_S) of the post-annealed bilayer films irradiated at different fluences, respectively. The resistivity value of the pristine samples was found to be high, which is ~85.32 ohm cm. The higher values of resistivity for the pristine sample may be due to the amorphous nature of Ge, containing a higher defect concentration, which is responsible for scattering of the charge carriers. The resistivity was found to decrease from 10.52 ohm cm to 2.17 ohm cm (see Table 2) after post-annealing of the irradiated samples, which may be due to the increase in the crystallization of Ge. The sheet resistance, which helps in studying the near surface crystallinity effect on resistance, was calculated using the formula $R_S = \frac{\rho}{t}$, where t is the thickness of the bilayer film. The sheet resistance of the pristine samples was found to be 8.53 mega-ohm per square, which decreased from 8.53 to 0.21 mega-ohm per square, confirming the crystallization of Ge.[38]

Based on the optical and electrical observations, we sketched a schematic energy band diagram of the separated Au metal and Ge, a-Ge/Au junction (*i.e.* pristine sample), and the post-annealed samples irradiated at fluence of 1×10^{12} ions per cm^2 and 5×10^{13} ions per cm^2, as shown in Fig. 10(a–d). Fig. 10(a) shows the individual energy band diagram of the Au metal and amorphous semiconductor (*i.e.* a-Ge), where φ_M and φ_S are the work functions of the metal and semiconductor ($\varphi_M > \varphi_S$), respectively, and q is the charge of carrier.[39] The Fermi level of the metal and semiconductor are denoted by E_{FM} and E_{FS}, respectively. The occupied states in Au and a-Ge are shown with blue titled dotted lines. a-Ge has many defect states (due to the presence of disorder) below the conduction band (CB) and above the valence band (VB) edge, which are shown with blue straight dotted lines, and exponentially extended energy states (*i.e.* density of state (DOS) tail) are present due to these defect states.[40] E_{g1} and E_{g2} are the energy gap of the defect states to the band edge, and CB edge to VB edge, respectively.[40,41] When we prepared the a-Ge/Au junction, shifting of the Fermi level occurred due to the work function difference between Au and a-Ge, which led to band bending, as shown in Fig. 10(b). Fig. 10(c) shows the energy band diagram of the post-annealed samples irradiated at a fluence of 1×10^{12} ions per cm^2. The a-Ge/Au interface will be rough due to the interface diffusion of Au and Ge atoms during irradiation and annealing. This figure shows a lower number of a-Ge defect states since a-Ge was crystallized. The conduction band edge shifts downwards, and valence band edge shifts upwards due to the reduction in defect states and increase in the crystallinity of Ge.[41,42] On the other hand, some defect states of Au (red dotted lines) were introduced within the band gap of Ge due the interface diffusion of Au after the crystallization of Ge. As an impurity, the Au atom may change the bond length of Ge, which leads to the formation of defect states.[37,43,44] The crystallization of Ge and formation of Au defect states in the original band gap of Ge leads to the formation of a new band gap of Ge, which was found to decrease in the post-annealed samples irradiated at different fluences, as observed in the optical absorption (see Fig. 8). The band gaps of c-Ge and a-Ge are $E'_g = (2E'_{g1} - E'_{g2})$ and $E_g = (2E_{g1} - E_{g2})$, respectively. It was experimentally observed that the energy band gap for c-Ge (E'_g) is less than that of a-Ge (E_g).[40] It should be noted here that Au is monovalent, which renders crystallized Ge as intrinsic, as confirmed by the Hall measurement. Fig. 10(d) shows the band diagram of the post-annealed samples irradiated at a high fluence of 5×10^{13} ions per cm^2. The number of defect states is much less since Ge is highly crystalline (see the figure). As a result, the conduction band edge and valence band edge are shifted more downward and upward, respectively. The

Table 2 The crystalline volume fraction of Ge (X_c), band gap of bilayer system, resistivity, and sheet resistance of the films

Sample details	X_c of Ge (%)	Band gap of Ge (eV)	Resistivity (ohm cm)	Sheet resistance (mega ohm per square)
Pristine	0	0.85	85.32	8.53
1×10^{12} ion-cm^{-2} + annealed at 300 °C	82.48	0.79	10.52	1.05
5×10^{12} ion-cm^{-2} + annealed at 300 °C	87.33	0.72	6.78	0.67
1×10^{13} ion-cm^{-2} + annealed at 300 °C	89.27	0.69	3.89	0.38
5×10^{13} ion-cm^{-2} + annealed at 300 °C	90.78	0.64	2.17	0.21

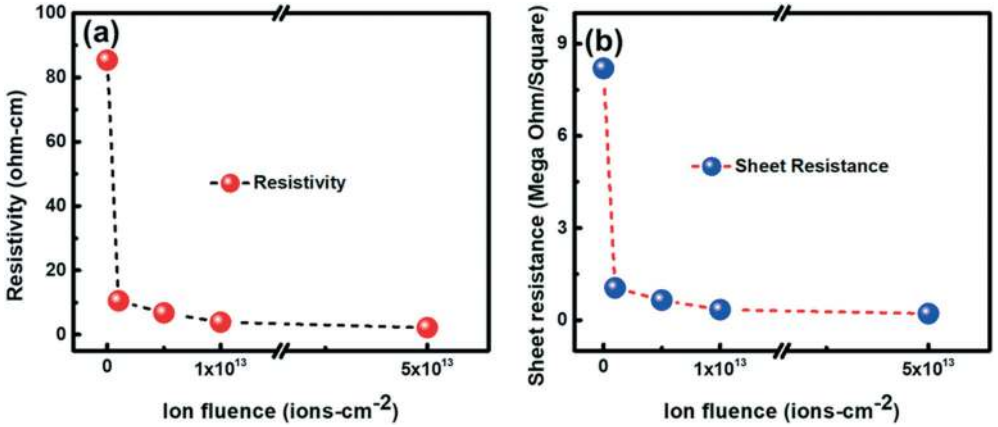

Fig. 9 (a) Resistivity and (b) sheet resistance of the pristine and post annealed (at 300 °C) samples after ion irradiation at different fluences.

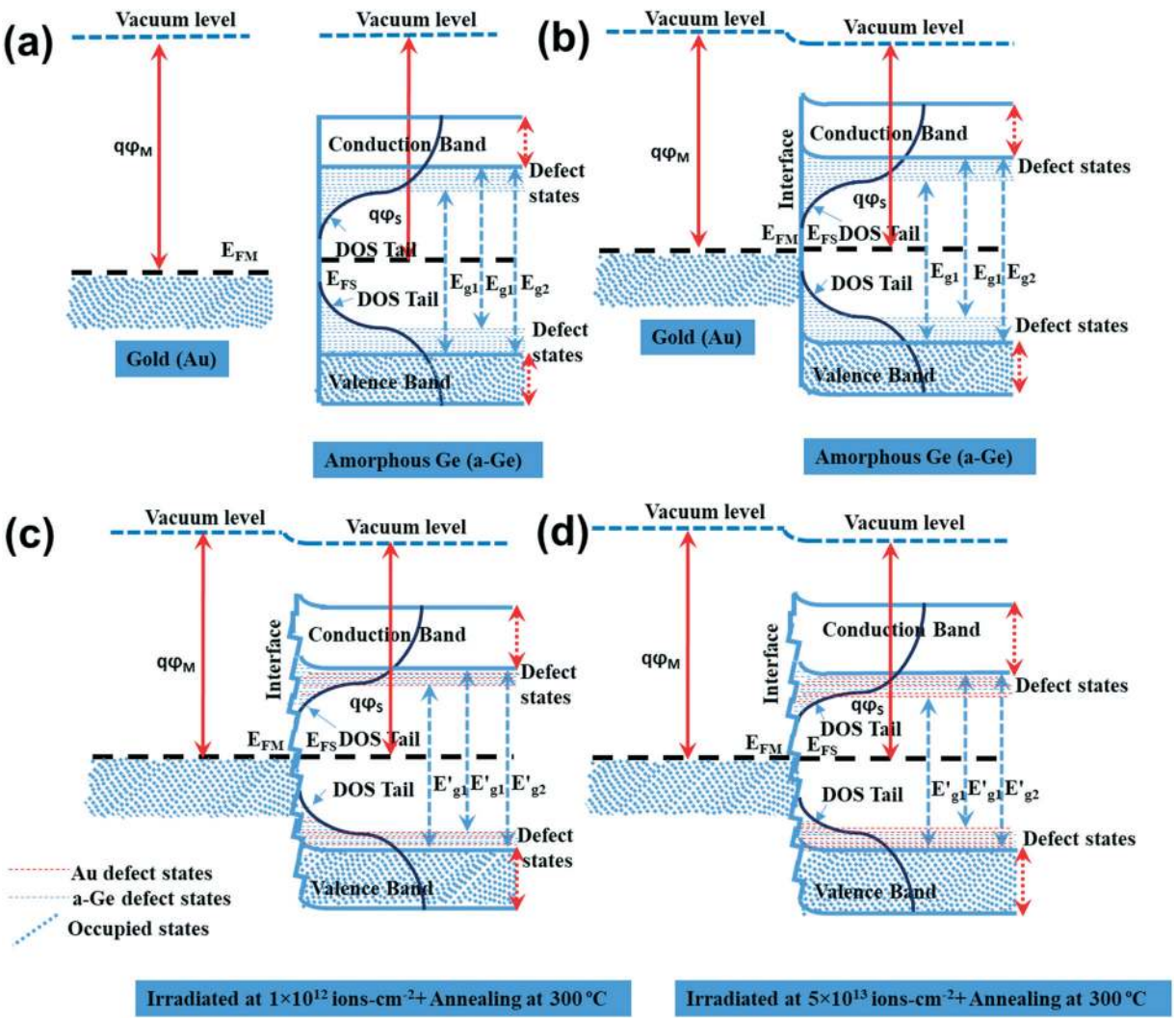

Fig. 10 Schematic energy band diagram of (a) separated Au metal and a-Ge (b) a-Ge/Au junction (*i.e.* pristine samples) and post-annealed (at 300 °C) after ion irradiation at different fluences of (c) 1×10^{12} ions per cm^2 and (d) 5×10^{13} ions per cm^2.

electrons in larger Ge crystallites will be confined in this volume, leading to the quantization of the electron levels in the conduction band and hole levels in the valence band, which results in the shifting of the band edges.[41,42] The defect states introduced in Ge band gap by Au are due to the high interface diffusion of Au and Ge at a higher

fluence. Briefly, it can be concluded that due to the higher crystallinity of Ge (which leads to a reduction in the a-Ge defect states) and higher interface diffusion of Au and Ge (Au introduces a greater number of defect states in Ge), the Ge band gap was found to be low.[37,42] The electrical resistivity of the pristine sample is high because of the trapping of charge carriers (due to the presence of a huge amount of defect states), which reduces the carrier lifetime, mobility, and diffusion length. The electrical resistivity values were found to be lower for the post-annealed samples irradiated at a higher fluence due to the reduction in the defect states of Ge and reduction in the band gap energy. The Au-induced defect states in the band gap will also be beneficial for electron transport from the valence band to conduction band.

IV. Conclusion

In conclusion, the Au-induced crystallization of a-Ge was studied after post-annealing of samples irradiated at different ion fluences in the range of 1×10^{12} ions per cm^2 to 5×10^{13} ions per cm^2. The effect of Au crystallite size on the crystallization of Ge was investigated. The ion beam irradiation modified the crystallites size of Au, which was found to decrease with an increase in the ion fluence. The presence of smaller Au crystallites resulted in an increase in density of defect sinks (*i.e.* grain boundaries). The post-annealing of the ion-irradiated samples led to the crystallization of Ge. It was observed that the post-annealed samples irradiated at a higher fluence showed a higher degree of crystallinity. The present investigation may be useful for the research community in developing methodologies to control the crystal growth of Ge by selectively introducing a desired concentration of defect sinks at a desired location or pattern in the material using ion irradiation before annealing.

Conflicts of interest

There is no conflict of interest exists.

Acknowledgements

The authors are thankful to Dr. D. Kabiraj for helping in thin film deposition at IUAC, New Delhi. Help received from Mr. Alapan Dutta, IOP Bhubaneswar at the time of UV-visible measurement is acknowledged. One of the author (GM & SPP) is also thankful to Inter University Accelerator Center, New Delhi for providing the fellowship through UFUP project (UFR-58308) to carry out this work. DK is thankful to DAE of India for the award of Raja Ramanna Fellowship.

SPP is thankful to the UGC and DST, Government of India, New Delhi for supporting the Department of Pure and Applied Physics through UGC-SAP, DRS-1 and FIST Level-1 program, respectively. Authors are thankful to IUAC, New Delhi for extending FESEM facility, funded by MoES under Geochronology project.

References

1 T. Nagashima, K. Okumura, K. Muratal and M. Yamaguchi, *A germanium back contact type cell for thermo-photovoltaic applications, Proceedings of the Third World Conference on Photovoltaic Energy Conversion, Osaka, Japan*, 2003, pp. 200–203.

2 R. R. King, D. C. Law, K. M. Edmondson, C. M. Fetzer, G. S. Kinsey, H. Yoon, R. A. Sherif and N. H. Karam, 40% efficient metamorphic GaInP/GaInAs/Ge multi-junction solar cells, *Appl. Phys. Lett.*, 2007, **90**, 183516–183519.

3 C. Becker, D. Amkreutz, T. Sontheimer, V. Preidel, D. Lockau, J. Haschke, L. Jogschies, C. Klimm, J. J. Merkel, P. Plocica, S. Steffens and B. Rech, Polycrystalline silicon thin-film solar cells: status and perspectives, *Sol. Energy Mater. Sol. Cells*, 2013, **119**, 112–123.

4 K. Toko, R. Yoshimine, K. Moto and T. Suemasu, High-hole mobility polycrystalline Ge on an insulator formed by controlling precursor atomic density for solid-phase crystallization, *Sci. Rep.*, 2017, **07**, 16981–16986.

5 D. Takahara, K. Moto, T. Imajo, T. Suemasu and K. Toko, Sb-doped crystallization of densified precursor for n-type polycrystalline Ge on an insulator with high carrier mobility, *Appl. Phys. Lett.*, 2019, **114**, 082105–082110.

6 H. Takiguchi, Z. Yoshikawa, H. Miyazaki, Y. Okamoto and J. Morimoto, The role of Au in the thermoelectric properties of amorphous Ge/Au and Si/Au thin films, *J. Electron. Mater.*, 2010, **39**, 1627–1633.

7 P. Wang, H. Liu, D. Qi, Q. Q. Sun, S. Chen, C. Li, W. Huang and H. Lai, Influence of order degree of amorphous germanium on metal induced crystallization, *J. Cryst. Growth*, 2015, **416**, 106–112.

8 H. Miyazaki, H. Takiguchi, M. Aono and Y. Okamoto, Influence of annealing temperature and Au concentration on the electrical properties of multilayered a-Ge/Au films, *J. Non-Cryst. Solids*, 2012, **358**, 2103–2106.

9 C. N. Yeh, K. Yang, H. Y. Lee and A. T. Wu, Elucidating the metal-induced crystallization and diffusion behavior of Al/a-Ge thin films, *J. Electron. Mater.*, 2012, **41**, 159–165.

10 D. Pelati, O. Mauguin, L. Largeau, F. Brisset, F. Glas and F. Oehler, Kinetics and crystal texture improvements on thin germanium layers obtained by aluminium induced crystallization using oxygen plasma, *Surf. Coat. Technol.*, 2017, **343**, 121–126.

11 R. Yoshimine, K. Toko, N. Saitoh, N. Yoshizawa and T. Suemasu, Silver-induced layer exchange for polycrystalline germanium on a flexible plastic Substrate, *J. Appl. Phys.*, 2017, **122**, 215305–215310.

12 M. Nakata, K. Toko and T. Suemasu, Effects of Al grain size on metal-induced layer exchange growth of amorphous Ge thin film on glass substrate, *Thin Solid Films*, 2017, **626**, 190–193.

13 J. H. Park, K. Kasahara, K. Hamaya, M. Miyao and T. Sadoh, High carrier mobility in orientation-controlled large-grain (≥50 μm) Ge directly formed on flexible plastic by nucleation-controlled gold-induced-crystallization, *Appl. Phys. Lett.*, 2014, **104**, 252110–252114.

14 K. Toko, R. Numata, N. Oya, N. Fukata, N. Usami and T. Suemasu, Low-temperature (180 °C) formation of large-grained Ge (111) thin film on insulator using accelerated metal-induced crystallization, *Appl. Phys. Lett.*, 2014, **104**, 022106–022109.

15 J. Y. Wang, D. He, Y. H. Zhao and E. J. Mittemeijer, Wetting and crystallization at grain boundaries: origin of aluminum-induced crystallization of amorphous silicon, *Appl. Phys. Lett.*, 2006, **88**, 061910–061912.

16 M. Nakata, K. Toko and T. Suemasu, Effects of Al grain size on metal-induced layer exchange growth of amorphous Ge thin film on glass substrate, *Thin Solid Films*, 2017, **626**, 190–193.

17 Y. K. Mishra, D. K. Avasthi, P. K. Kulriya, F. Singh, D. Kabiraj, A. Tripathi, J. C. Pivin, I. S. Bayer and A. Biswas, Controlled growth of gold nanoparticles induced by ion irradiation: An in situ x-ray diffraction study, *Appl. Phys. Lett.*, 2007, **90**, 073110–073112.

18 Y. K. Mishra, D. Kabiraj, D. K. Avasthi and J. C. Pivin, Swift heavy ion-induced dissolution of gold nanoparticles in silica matrix, *Radiat. Eff. Defects Solids*, 2007, **162**, 207–213.

19 J. F. Ziegler, J. P. Biersack and U. Littmark, *The stopping and range of ions in solids*, Pergamon, New York, 1985.

20 L. R. Doolittle, Algorithms for the rapid simulation of Rutherford backscattering spectra, *Nucl. Instrum. Methods Phys. Res., Sect. B*, 1985, **9**, 344.

21 S. P. Patel, J. C. Pivin, G. Maity, R. P. Yadav, R. Chandra, D. Kanjilal and L. Kumar, Microstructural and surface morphological studies on Co doped ZnS diluted magnetic semiconductor thin films, *J. Mater. Sci.: Mater. Electron.*, 2018, **29**, 13541–13550.

22 S. I. Fujikawa, K. I. Hirano and Y. Fukushima, Diffusion of silicon in aluminum, *Metall. Trans. A*, 1978, **9**, 1811–1815.

23 T. Som, P. Ayyub, D. Kabiraj, N. Kulkarni, V. N. Kulkarni and D. K. Avasthi, Formation of Au0.6Ge0.4 alloy induced by Au-ion irradiation of Au/Ge bilayer, *J. Appl. Phys.*, 2003, **93**, 903–906.

24 Z. M. Wang, J. Y. Wang, L. P. H. Jeurgens and E. J. Mittemeijer, Thermodynamics and mechanism of metal-induced crystallization in immiscible alloy systems: experiments and calculations on Al/a-Ge and Al/a-Si bilayers, *Phys. Rev. B: Condens. Matter Mater. Phys.*, 2008, **77**, 045424–045439.

25 S. Peng, D. Hu and D. He, Low-temperature preparation of polycrystalline germanium thin films by Al-induced crystallization, *Appl. Surf. Sci.*, 2012, **258**, 6003–6006.

26 M. Jiang and D. Ahn, Seed-induced crystallization of polycrystalline germanium thin films at low temperature, *Results Phys.*, 2019, **14**, 102502–102503.

27 T. Okada, T. Iwaki, H. Kasahara and K. Yamamoto, Probing the Crystallinity of Evaporated Silicon Films by Raman Scattering, *Jpn. J. Appl. Phys.*, 1985, **24**, 161–165.

28 C. K. Singh, T. Tah, K. K. Madapu, K. Saravanan, S. Ilango and S. Dash, Au induced crystallization and layer exchange in a-Si/Au thin film on glass below and above the eutectic temperature, *J. Non-Cryst. Solids*, 2017, **460**, 130–135.

29 R. P. Yadav, T. Kumar, V. Baranwal, M. Vandana, P. K. Kumar, S. N. Priya and A. K. Mittal, Fractal characterization and wettability of ion treated silicon surfaces, *J. Appl. Phys.*, 2017, **121**, 055301.

30 G. Maity, S. Ojha, I. Sulania, K. Devrani and S. P. Patel, Fractal characterizations of energetic Si ions irradiated amorphized Si surfaces, *Surf. Interface Anal.*, 2019, **51**, 817–825.

31 M. V. Berry and I. C. Percival, Optics of Fractal Clusters Such as Smoke, *Opt. Acta*, 1986, **33**, 577–592.

32 M. Gerosal and C. E. Bottani, Multiple light scattering and near-field effects in a fractal treelike ensemble of dielectric nanoparticles, *Phys. Rev. B: Condens. Matter Mater. Phys.*, 2013, **87**, 195312–195320.

33 C. Y. Tsao, J. W. Weber, P. Campbell, G. Conibeer, D. Song and M. A. Green, In situ low temperature growth of poly-crystalline germanium thin film on glass by RF magnetron sputtering, *Sol. Energy Mater. Sol. Cells*, 2010, **94**, 1501–1505.

34 A. Axelevitch, V. Eidin and B. Gorenstein, Effect of Photothermal Treatment on Properties of Ge Thin Films, *J. Mater. Sci. Eng. A*, 2013, **3**, 475–480.

35 F. Kezzoula, A. Hammouda, M. Kechouane, P. Simon, S. E. H. Abaidia, A. Keffous, R. Cherfi, H. Menari and A. Manseri, Aluminium-induced crystallization of amorphous silicon films deposited by DC magnetron sputtering on glasses, *Appl. Surf. Sci.*, 2011, **257**, 9689–9693.

36 D. Song, E. C. Cho, G. Conibeer, C. Flynn, Y. Huang and M. A. Green, Structural, electrical and photovoltaic characterization of Si nanocrystals embedded SiC matrix and Si nanocrystals/c-Si heterojunction devices, *Sol. Energy Mater. Sol. Cells*, 2008, **92**, 274–481.

37 A. R. Zanatta and M. E. Kordesch, On the structural-optical properties of Al-containing amorphous Si thin films and the metal-induced crystallization phenomenon, *J. Appl. Phys.*, 2014, **116**, 073511–073518.

38 I. Kabacelik, M. Kulakci, R. Turan and N. Unal, Effects of gold-induced crystallization process on the structural and electrical properties of germanium thin films, *Surf. Interface Anal.*, 2018, **50**, 744–751.

39 H. B. Michaelson, The work function of the elements and its periodicity, *J. Appl. Phys.*, 1977, **48**, 4729–4733.

40 S. G. Tomlin, E. Khawaja and G. K. M. Thutupalli, The optical properties of amorphous and crystalline germanium, *J. Phys. C: Solid State Phys.*, 1976, **9**, 4335.

41 M. S. Tyagi, *Introduction to semiconductor materials and devices*, Wiley, 2008, p. 688.

42 T. van Buuren, L. N. Dinh, L. L. Chase, W. J. Siekhaus and L. J. Terminello, Changes in the electronic properties of Si nanocrystals as a function of particle Size, *Phys. Rev. Lett.*, 1998, **80**, 3803–3806.

43 W. C. Dunlap Jr., Gold as an Acceptor in Germanium, *Phys. Rev.*, 1955, **97**, 614–629.

44 M. F. Millea, The effect of doping on gold diffusion in germanium, *J. Phys. Chem. Solids*, 1966, **27**, 309–314.

